ACSNANO

www.acsnano.org

ARTICLE

Atomistic Imaging of Competition between Surface Diffusion and Phase Transition during the Intermetallic Formation of Faceted Particles

Fan Li, Yuan Zong, Yanling Ma, Mingxu Wang, Wen Shang, Peng Tao, Chengyi Song, Tao Deng, Hong Zhu,* and Jianbo Wu*

Cite This: *ACS Nano* 2021, 15, 5284–5293

Read Online

ACCESS | Metrics & More | Article Recommendations | Supporting Information

ABSTRACT: To explore the ordering mechanism of facet alloy nanocrystals with randomly distributed atoms, we investigate kinetic and thermodynamic behaviors of the ordering phase transition from face-centered cubic Pt_3Co nanocrystals to $L1_2$-Pt_3Co intermetallic nanocrystals. It is observed that the ordering occurs from the surface and then gradually into the interior in a layer-by-layer mode, involving the competition between two kinds of phase transition modes: long-range surface diffusion-induced phase transition (SDIPT) and short-range reconstruction-induced body phase transition (RIBPT). The density functional theory calculations demonstrate that the surface status acts as a pivotal part in the thermodynamics and kinetics of the nanoscale ordering transition. With the development of the controllable heating process, both SDIPT and RIBPT modes can be manipulated as well as the morphology of the final product. This *in situ* work lays the foundations for potentially realizing shape-controlled intermetallic nanostructures by utilizing the thermal annealing method and makes preparations for the rational design of the surface and near-surface atomic configurations at the atomic scale.

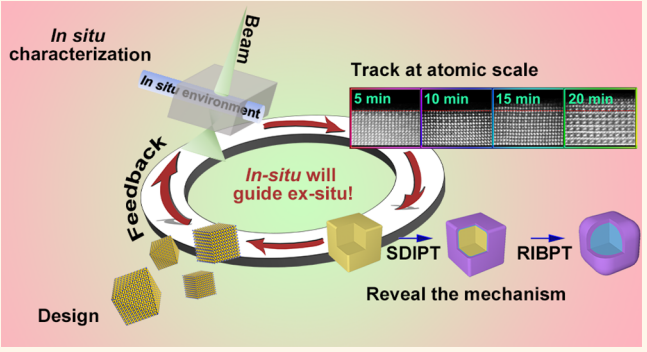

KEYWORDS: *in situ atomic STEM images, nanometallurgy, surface diffusion, phase transition of intermetallics, shape-controlled intermetallic nanostructures*

Nanoscale metallurgy, involving the liquidation, surface segregation, phase transition, and diffusion, is attracting more and more attention, because it is generally applied in the rational design and preparation of metallic-based nanocatalysts,[1−3] which are widely used in various electrochemical applications including oxygen reduction reaction (ORR),[4−17] oxygen evolution reaction,[18] hydrogen oxidation reaction,[19] and hydrogen evolution reaction.[20] The aforementioned metallurgical behaviors have been extensively discussed for bulk materials in the past hundred years. However, when applying those classic theories into the nanoscale, we found most of them could not be applicable. For example, the melting point is largely reduced at the nanoscale.[21] In addition, the surface segregation, phase transition, and diffusion behaviors of nanoparticles (NPs) are very different from those of bulk materials.[21,22] All these changes make the nanometallurgy not easy to understand *via* utilizing the existing classic theory. Also, the related detailed theoretical and experimental studies are mostly under development, especially those on the eutectic point and phase transition temperature in the equilibrium phase diagrams of NPs.[22−26]

Interestingly, the surface optimization of nanocatalysts and well-defined stoichiometric intermetallics are presently attracting considerable research attention because of their special and excellent performance.[2,3,27−37] The ORR activity of Pt_3Ni icosahedral NPs stretching 20 tetrahedrons is 9 times higher

Received: December 23, 2020
Accepted: February 16, 2021
Published: February 19, 2021

https://dx.doi.org/10.1021/acsnano.0c10775
ACS Nano 2021, 15, 5284–5293

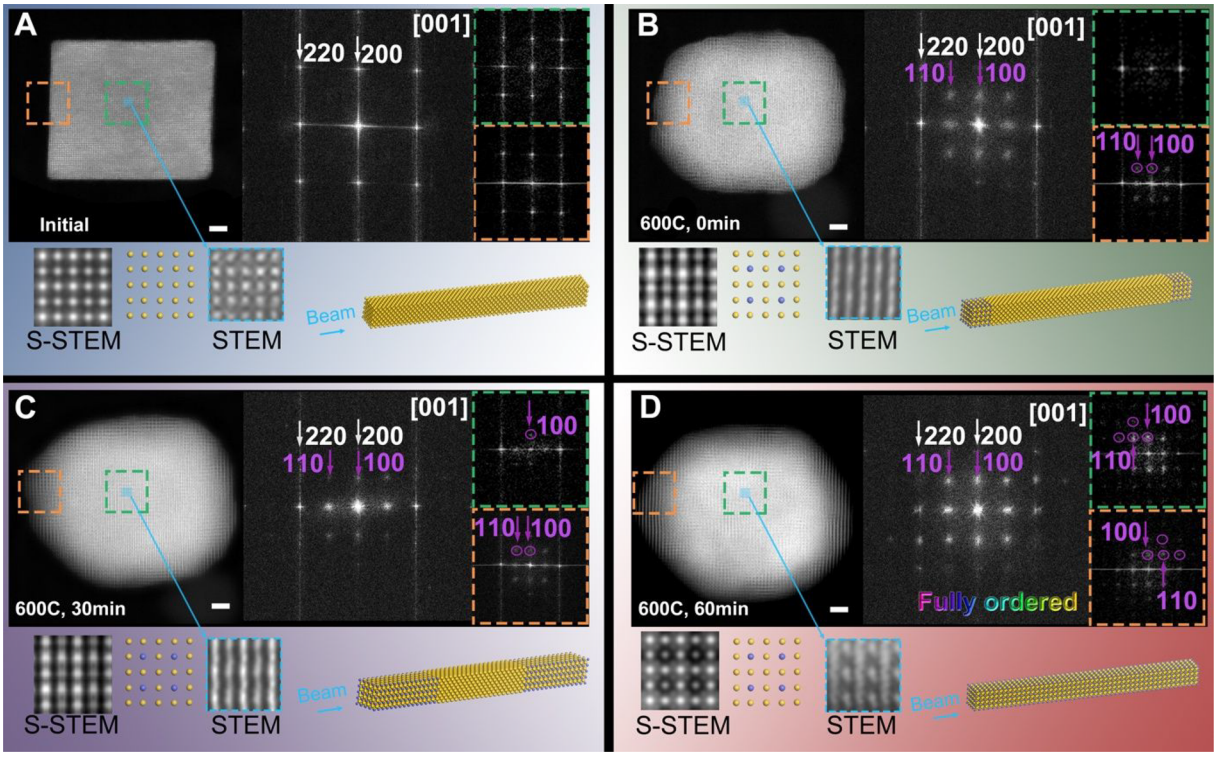

Figure 1. ***In situ*** **HAADF-STEM images and the corresponding FFT, simulated HAADF-STEM (S-STEM) images, and schematic slab model of Pt_3Co cube annealed at different temperatures and time. (A) Initial Pt_3Co cube at RT. (B) Temperature increased to 600 °C with a heating rate of 30 °C/min and maintained for (C) 30 min at 600 °C and (D) 60 min at 600 °C. The FFT (pattern without rectangle) is the overall FFT of the corresponding HAADF-STEM images. The green square area indicates the separate FFT in the center of the Pt_3Co NP, while the orange square area indicates the separate FFT on the surface of Pt_3Co NP. The corresponding S-STEM images were simulated utilizing the (100) slab models with their separated ordering layers. The enlarged filtered STEM images were inserted in the blue dashed square for comparison with STEM. The fully ordered structure is observed in (D). Scale bar, 2 nm.**

than the commercial Pt/C catalyst.[35,36] It was reported the ordered intermetallic phase had improved the durability and activity of electrocatalysts compared with random alloys.[7,8,10,12,13] If the optimized facet intermetallic NPs can be prepared, then both of high electrocatalytic activity and good durability will be achieved. Indeed, the formation of intermetallics is achieved through thermal annealing above the eutectic point, which has been considered as one of the promising strategies. However, synthesizing facet- and shape-controlled intermetallic nanocrystals with elemental ordering is really a challenging issue because the formation of intermetallics at the elevated temperature required a certain level of atom migration, which also leads to a side effect of surface changes.[38] Chi *et al.* have reported that the disorder-to-order phase transformation occurred at 600 °C for the Pt_3Co spherical NPs, which was lower than that reported for bulk Pt_3Co (~750 °C)[39,40] because of a higher elemental internal migration rate,[38] although the surface changes have not been studied yet. Their *in situ* studies of the intermetallics' formation focused on spherical NPs, which are almost isotropic on the surface with negligible surface diffusion during annealing. Andreazza *et al.* have reviewed the size effects and surface segregation during phase transition on the bulk materials and NPs of the CoPt system on the basis of theoretical studies, even if they did not pay attention to the facet effect.[41] Considering the faceted particles (cube, octahedron, and icosahedron) with the anisotropic surface, the thermal annealing process was often accompanied by the change of morphology and shape because of surface atom diffusion.[2,7] Thus, the thermal annealing techniques to obtain shape-controlled bimetallic intermetallic NPs had received limited achievement so far.[2] The key challenge for the synthesis of the desired geometry aiming for the optimized performance is how the surface could be maintained during the thermal annealing process. Therefore, the insight on ordering behavior about faceted particles accompanying the surface diffusion during annealing is critical to developing the surface preserved annealing process.

Here, we reveal the surface diffusion behaviors in the dynamics of Pt_3Co intermetallic formation from a Pt_3Co alloy cube during the annealing process *via in situ* scanning transmission electron microscopy (STEM). By tracking the dynamic ordering transitions at the atomic scale, the different triggers and behaviors of phase transition on (100) and (110) and element diffusion behavior around corners and edges have been studied during different annealing processes. This work will make it easier to achieve regulation of morphology and elemental ordering during various annealing processes for optimization of the intermetallics.

RESULTS AND DISCUSSION

The presynthesized Pt_3Co cubes (Figure S1) were dispersed on a carbon film thermal E-chips with 9 μm holes. The *in situ* annealing experiments were carried out in a JEOL JEM-ARM200F Cs corrected STEM. Figure 1A clearly shows that the initial Pt_3Co NP has a cubic shape with an edge length of ~18 nm, projected along the zone axis of [001]. The corresponding fast Fourier transform (FFT) pattern in the

https://dx.doi.org/10.1021/acsnano.0c10775
ACS Nano 2021, 15, 5284−5293

inset of Figure 1A only appears on {200} and {220} planes but does not appear on {100} and {110} planes, which confirms that the Pt_3Co cube has a disordered face-centered cubic (FCC) alloy structure.[7,42−45] The Pt_3Co NP exhibits a homogeneous random elemental distribution (see Figure S2) at room temperature (RT) with a composition of 75.78:24.22 for Pt:Co (EDS; see Figure S3). In the slow heating process, the Pt_3Co cubic NP was preannealed at 300 °C, at which the Pt_3Co NPs could diffuse adequately but not occur at the phase transition.[24] After proceeding for 60 min, the cubic structure was slightly changed with the rounded corner (see Figure S4A) due to the surface diffusion of low-coordination (CN) atoms. However, the FFT in Figure S4A only with the original facet index {200} and {220} still illustrates a pure FCC structure, indicating that the phase transition did not occur at 300 °C. When we increased the temperature to 400 and 500 °C, the corresponding FFT of the FCC structure in Figure S4B,C revealed that the phase transition had not been triggered yet, while the cubic structure became round. This phenomenon supports the previously reported results of both *ex situ* and *in situ* experiments.[38] When we increased the temperature to 600 °C, a more dramatic diffusion from the corner to the {100} terrace leads to the formation of a rounder structure. Meanwhile, some additional diffraction points appear in the FFT on the surface region of the Pt_3Co NP (Figure 1B), which are assigned as the {100} and {110} points of the $L1_2$-Pt_3Co intermetallic nanocrystals.[7,43−45] Obviously, the $L1_2$ transition started on the surface at 600 °C. To distinguish whether the body region covered by two layers of (100) surfaces has a fully ordered structure, we do the simulated high-angle annular dark-field (HAADF)-STEM (S-STEM) utilizing quantitative STEM (QSTEM) simulations. Combined with the S-STEM images (Figure 1 and Figure S5), we can roughly estimate the thickness of the intermetallic compounds that coexist with disordered FCC Pt_3Co nanocrystals in their body region. We observed that these representative ordered diffractions points including {100} and {110} only appear in the surface region but not the body region (Figure 1B). In addition, the STEM image in the body region in Figure 1B displayed a uniform brightness, which indicated the fully ordered structure had not been formed in the body region. The thickness of intermetallic compounds increases gradually layer-by-layer from the surface during the annealing at 600 °C for 30 min on the basis of the corresponding inner FFT and S-STEM images (Figure 1C and Figure S5). Finally, the fully ordered $L1_2$-Pt_3Co intermetallic spherical NPs (Figure 1D and Figure S6) were achieved after annealing at 600 °C for more than 60 min, which was confirmed by the additional {100} and {110} diffraction in both of the surface and body regions (Figure 1D). The ordered $L1_2$-Pt_3Co intermetallic nanocrystals after annealing exhibits a slight change in the elemental composition (Figures S6 and S7) compared to disordered FCC Pt_3Co nanocrystals (Figures S2 and S3), where the ratio of Pt:Co changed to 3.05:1 compared with the initial ratio of 3.13:1.

The detailed structure and morphology progression of a random FCC alloy Pt_3Co nanocube to an ordered $L1_2$ phase Pt_3Co spherical NPs has been characterized clearly during *in situ* annealing. With the evolution of the surface geometry, we also investigated the accompanying dynamics of phase transition at the atomic resolution. After the alignment of the series of sequential STEM (Figure S8), we discovered that the phase transition with facet change involved two types of processes: (1) one *via* surface diffusion of the atoms from corner to {100} terrace (surface diffusion-induced phase transition (SDIPT) mode) and (2) the other is due to the internal reconstruction from disordered FCC nanocrystals to ordered $L1_2$ intermetallic nanocrystals (reconstruction-induced body phase transition (RIBPT) mode). The SDIPT mainly occurs in the surface layer, involving a long-range diffusion derived by the chemical potential gradient on the surface. For the RIBPT, these atoms can reconstruct inside the crystal within a short range. The obvious characteristic is that RIBPT does not change the NPs' shape, but it occurs at a higher temperature. We observed that the phase transition on the {100} surface was the combination of those two modes (Figure S8), and the interaction between SDIPT and RIBPT ultimately controls the dynamics of structural and shaped changes. We have differentiated these two modes through the alignment line (see the details in the caption of Figure S8). In the beginning, the growth rate of intermetallics from SDIPT (1.6 layers/min) is faster than the RIBPT (1.2 layers/min) at stage I (Figure 2). At stage II when the SDIPT is eliminated

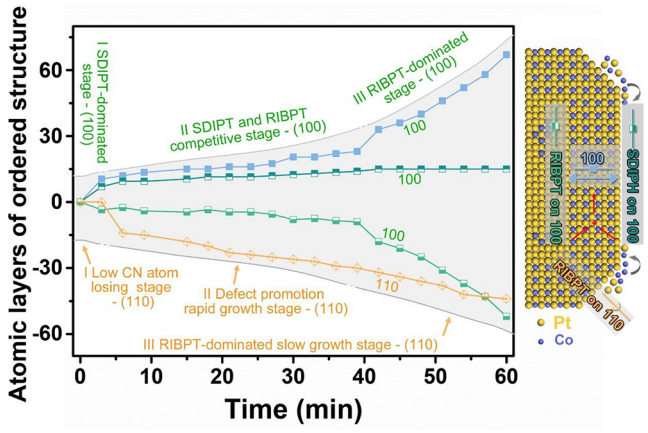

Figure 2. Reconstruction and surface-diffusion-induced phase transition behavior under 600 °C along the direction of Pt_3Co [100] and [110]. Changes of atomic layers of the ordered $L1_2$-Pt_3Co intermetallic nanocrystals along [100] and [110] directions as a function of time, respectively. The ordering behaviors along [100] and [110] directions were separately divided into three stages. (See Figure S8 for the example of alignment of the corresponding HAADF-STEM images and profiles.)

due to the disappearance of diffusion from the corner in the truncated octahedron, the growth rate of the intermetallics from RIBPT (0.2 layers/min) is almost equal to the SDIPT (0.2 layers/min) (Figure 2 and Table S1). Then the growth rate of intermetallics from RIBPT (2.0 layers/min) is far greater than that of SDIPT at stage III, which has stopped growing due to lack of diffusion atoms (Figure 2 and Table S1). This growth rate for the intermetallics from RIBPT at stage III is rapid because the reconstruction becomes easier after leaping over the barrier of nucleation at stage II.[46−48] Above all, we could conclude three growth stages on (100) as SDIPT-dominated stage (stage I), SDIPT and RIBPT competitive stage (stage II), and RIBPT-dominated stage (stage III) (Figure 2).

On the (110) surface, the triggering of the phase transition is later behind that on (100) because the corner atoms with low CN prefer to diffuse away instead of self-reconstruction. Most interestingly, the RIBPT along the ⟨110⟩ direction grew rapidly once started with a growth rate of 4.7 layers/min (Figure 2 and

https://dx.doi.org/10.1021/acsnano.0c10775
ACS Nano 2021, 15, 5284−5293

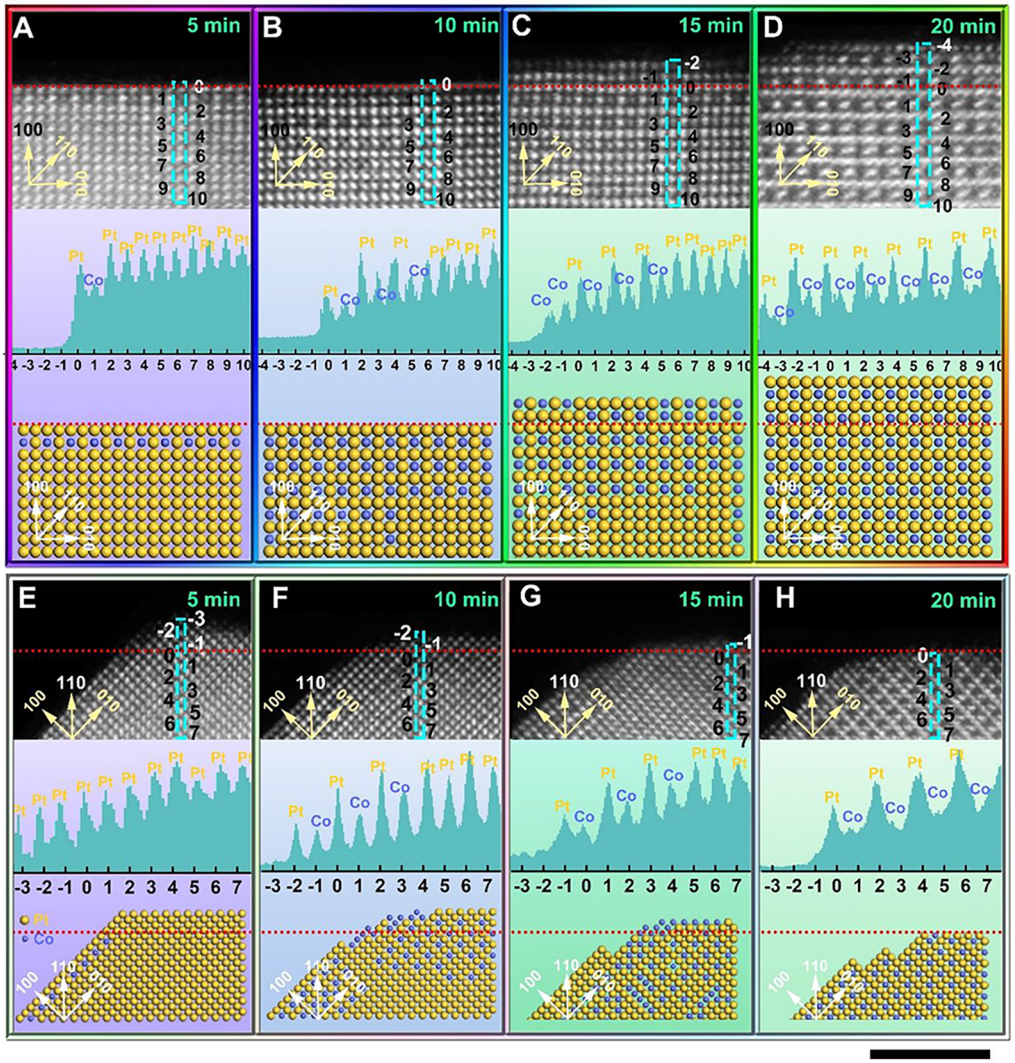

Figure 3. Layer-by-layer growth of the ordering Pt_3Co during annealing. Enlarged HAADF-STEM images of the (100) surface, the intensity profiles taken from the surface marked by rectangles and the corresponding atomic model of enlarged HAADF-STEM images acquired at 700 °C for (A) 5 min, (B) 10 min, (C) 15 min, and (D) 20 min along (100) surface and for (E) 5 min, (F) 10 min, (G) 15 min and (H) 20 min along the (110) surface. Scale bar is equal to 2 nm. (See Figures S12−S19 for the corresponding HAADF-STEM images, profiles, and atomic model.)

Table S1) at stage II, which is faster than the maximum growth rate along ⟨100⟩ (2.8 layers/min, stage I) (Figure 2 and Table S1). This rapid growth rate can be explained by the disappearance of corner atoms leaves a big density of vacancies and defects. In general, it was reported that surface defects and vacancies would accelerate the ordering and diffusion process because the loose surface full of defects would accelerate the atom-transport process with a lower formation energy of defect and jumping barrier.[2,10,49,50] Therefore, reconstruction along the {110} surface becomes easier once it begins.[2,49,50] After vigorous growth, the growth rate of intermetallics from the RIBPT along ⟨110⟩ direction at stage III (0.6 layers/min) becomes lower as it grows deeper with fewer vacancies and defects; however, it is still faster than the simultaneous growth rate of (100) (0.4 layers/min) (Figure 2 and Table S1). This difference in the growth rates is due to the different portions of the interstitial space on the different facets. The minimum ratio of interstitial space on the surface of Pt_3Co {100} (18.27% on layer B) is smaller than that of Pt_3Co {110} (18.84% on layer B), and the maximum ratio of space on the surface of Pt_3Co {100} (26.09% on layer A) is smaller than that of Pt_3Co {110} (47.74% on layer A), which makes atoms diffusion through the {110} surface easier than {100} (Figure S9).[51,52] Based on the atomic imaging of phase transition, we could define three growth stages on (110) as the low CN atoms losing stage (stage I), the defect promotion rapid growth stage (stage II), and the RIBPT-dominated slow growth stage (stage III) (Figure 2).

As we demonstrated, the diffusion promoted *via* the low-temperature aging could largely influence the behavior of phase transition. We further investigate the phase transition mechanism at the direct high-temperature annealing process (DHTAP) (Figure 3) by annealing the Pt_3Co nanocube under 700 °C directly (with a heating rate of 30 °C/min). It is interesting that without the low-temperature pretreatment at 300 °C, direct heating to 600 °C would not lead to the ordering transition (Figure S10). The surface ordering transition under DHTAP could be triggered at 700 °C, which is still lower than the phase transition temperature of bulk materials (~750 °C).[40] After alignment (Figure S11) and

https://dx.doi.org/10.1021/acsnano.0c10775
ACS Nano 2021, 15, 5284−5293

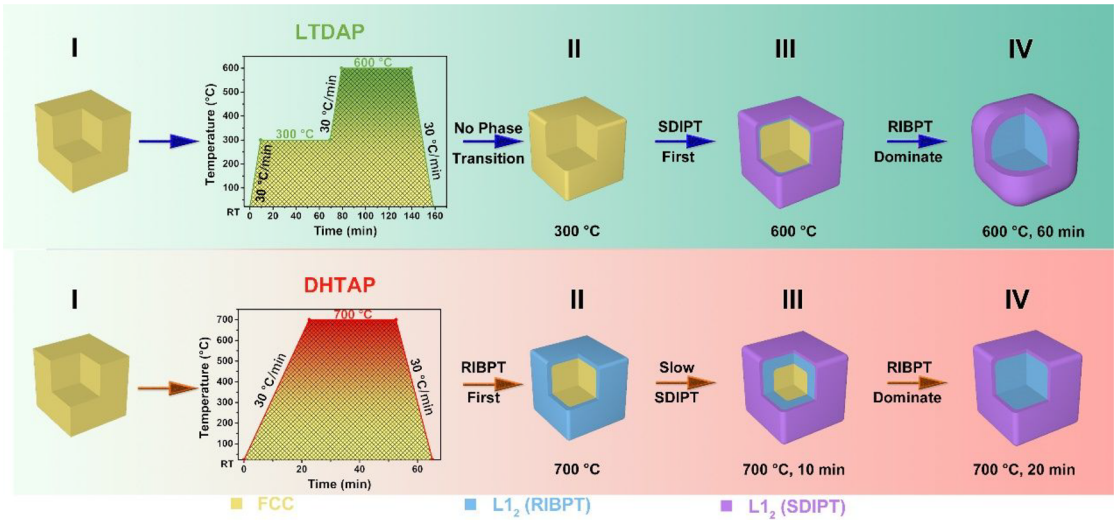

Figure 4. Schematic representation of the dynamic process of Pt_3Co cube under LTDAP and DHTAP. Under LTDAP, the $L1_2$-Pt_3Co intermetallic structure could not form at 300 °C (II) but then starts to form at 600 °C (III). This structure grows from the surface into the body, and eventually, the fully ordered $L1_2$-Pt_3Co intermetallic spherical nanocrystals appear (IV). As a comparison, under DHTAP, RIBPT starts first (II), and SDIPT gradually occurs behind RIBPT (III), and finally, the fully ordered $L1_2$-Pt_3Co truncated NPs form (IV).

the enlarged quantitative analysis (Figures S12–S19 and Figure 3), we observed that the ordered phase starts to form from the outermost layer of the (100) surface instead of the (110) surface at 700 °C after 5 min (Figure 3A,E), while there is no ordered phase appearing on the (110) surface until 10 min (Figure 3E,F). The big difference between the DHTAP and the low-temperature diffusion annealing process (LTDAP) is that the growth rate of intermetallics from SDIPT is slower than that of RIBPT without sufficient diffusion time at the initial stage of DHTAP and the cubic structure changed less during DHTAP compared with the spherical structure after LTDAP. According to the aligned HAADF-STEM images in the first 10 min (Figure 3A,B and Figure S10), we can observe that the surface ordered structures from RIBPT grow deeper on (100), but no SDIPT happened in that process because the atoms at the corner did not spread over the {100} terrace and the shape of the NP maintained relatively unchanged during the rapid heating process. With time over 15 min, the partially disordered atomic layers appear on the (100) terrace (Figure 3C), demonstrating that the corner atom diffused onto the (100) surface. Figure 3C also presents that these newly extra atoms, which diffused from the corner gradually, tend to form an ordered layer on the (100) surface. When the annealing time reached 20 min, all the atomic layers on the (100) and (110) surface become fully ordered (Figure 3D), and we observed a truncated cubic NP with sharper corners (Figure S11D). Indeed, the outmost four atomic layers on (100) are attributed to the surface diffusion, and the other is due to the reconstruction. We could also conclude the three growth stages of the surface ordering transition under DHTAP as the RIBPT-dominated stage (stage I, Figure 3A,E to Figure 3B,F), the SDIPT starting stage (stage II, Figure 3B,F to Figure 3C,G), and the SDIPT-RIBPT synergetic growth stage (stage III, Figure 3C,G to Figure 3D,H).

Above all, the main difference between LTDAP and DHTAP is the diffusion speed and phase transition rate. Under LTDAP, the $L1_2$-Pt_3Co intermetallic structure forms at the surface at a relatively low temperature (600 °C) and then grows from the surface into the body, and eventually the fully ordered $L1_2$-Pt_3Co intermetallic spherical nanocrystals form (Figure 4). We exhibited that a spherical structure with an almost round surface could be achieved during the complete ordering transition at 600 °C within 60 min *via* vigorous surface diffusion from the corner to the terrace. It is slightly lower than the predicted phase transition temperature (~650 °C) for the 18 nm Pt_3Co cube[24] and also lower than the temperature in the DHTAP because of the prolonged diffusion at the pretreatment stage at low temperature. We noticed that the surface of the cube after keeping 60 min at 300 °C became rough with a number of dangling atoms (Figure S4A). The results show that the loosed surface due to diffusion could make the surface ordering easier at a lower temperature. Unlike LTDAP, DHTAP could obtain a fully $L1_2$-Pt_3Co truncated cubic NP with sharper corners at a relatively higher temperature (~700 °C, Figure 3). As is shown in Figure 3, RIBPT starts first, and SDIPT gradually occurs behind RIBPT. Finally, the fully ordered $L1_2$-Pt_3Co truncated NPs could form. Considering the different heating procedures, the LTDAP promotes the diffusion of atoms from the corner to the surface, so this long-range diffusion makes SDIPT start earlier than the short-range RIBPT (Figure 4). The scenario becomes different under DHTAP, where RIBPT starts first on the (100) before the corner atoms diffuse to the (100) terrace. Above all, the entire particle becomes ordered around 20 min, which benefits from both the SDIPT and RIBPT. In general, the ordering under DHTAP (completed in 20 min) is faster than that under LTDAP (completed in 60 min), and both LTDAP and DHTAP induce SDIPT on the (100) surface and RIBPT on both the (100) and (110) surfaces (Figure 4). Although they have different phase transition rates at the various stages, intermetallics from SDIPT always produce a higher growth rate than that from RIBPT. We further quantify for the shape-controlled phase transition behaviors on the {100} surface utilizing the {100} facet preserved ratio in view of the 2D model and 3D model (see Supporting Information). As expected, the {100} facet preserved ratio in view of the two- and three-dimensional (2D and 3D) models of DHTAP (48.02% and 25.83%, respectively, Figures S20 and S21) is larger than that of LTDAP (32.63% and 9.58%, respectively, Figures S20 and S21), which was consistent with our

https://dx.doi.org/10.1021/acsnano.0c10775
ACS Nano 2021, 15, 5284–5293

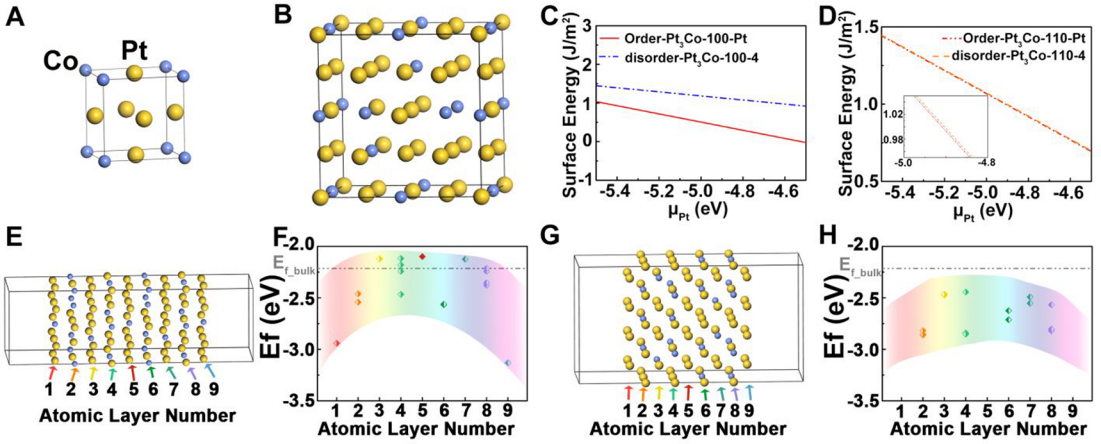

Figure 5. DFT simulation. (A) The atomic model of $L1_2$ Pt_3Co with FCC structure. (B) The atomic model of disordered Pt_3Co solid solution. (C) Dependence of the ordered and disordered (100) lowest surface energy on the chemical potential of Pt (μ_{Pt}). (D) Dependence of the ordered and disordered (110) lowest surface energy on μ_{Pt}. The enlarged region between −5.0 and −4.8 eV was inserted at the left corner. (E) The atomic model of disordered Pt_3Co (100) surface slab with atomic layer number labeled. (F) Dependence of Co vacancy formation energy (E_f) within the disordered Pt_3Co (100) surface slab on the atomic layer number (μ_{Pt} = −5.0 eV). (G) The atomic model of the disordered Pt_3Co (110) surface slab with the atomic layer number labeled. (H) Dependence of Co vacancy formation energy (E_f) within the disordered Pt_3Co (110) surface slab on the atomic layer number (μ_{Pt} = −5.0 eV).

observations. Last but not least, designing shape-controlled intermetallic nanostructures could be achieved by regulating the thermal annealing process based on *in situ* experimental results. Therefore, we believe a brand new shaped intermetallic structure can be obtained by rapid thermal processing of a shaped alloy, which could shorten SDIPT and further obtain the nanostructures with perfect corners and edges.

A density functional theory (DFT) simulation revealed the surface stability of all possible (100) and (110) surfaces, which were cleaved from the ordered $L1_2$ Pt_3Co model (Figure 5A) and disordered Pt_3Co solid solution models adopted in this work (Figure 5B). The DFT calculated surface energies of the possible {100} and {110} surfaces (Figures S22−S24) of disordered and ordered Pt_3Co were plotted as a function of the chemical potential of Pt (μ_{Pt}) (Figure S25). It is obvious that the lowest surface energy of the ordered (100) and (110) slab is lower than that of the disordered (100) and (110) slabs (Figure 5C,D), respectively. While the lowest surface energy difference between the ordered and the disordered (110) slab is very small, the lowest surface energy of the ordered (110) slab is lower than that of four possible disordered (110) surface slabs (Figure S25B,D). As a result, the ordering is thermodynamically favorable because the high-energy surface tends to reconstruct, react with each other, or adsorb the other small molecule to lower its surface energy. To further demonstrate the essence of the disordering−ordering phase transition, we calculated the vacancy formation energy (E_f) in the disordered Pt_3Co (100) and (110) slabs (Figure 5E,G), respectively. The lower vacancy formation energies will promote interdiffusion of the constituent atoms *via* a vacancy diffusion mechanism and further promote ordering.[53] The calculated E_f is plotted as a function of μ_{Pt} (Figure S27). Clearly, the Co atom always has a lower E_f than the Pt atom in the interior bulk region of disordered Pt_3Co (Figure S27). The results indicated that the diffusion of Co atoms dominated the ordering process, and then the detailed E_f (μ_{Pt} = 5.0 eV) calculation of Co vacancy within the Pt_3Co (100) and (110) surface slabs as a function of the distance from the surface was further carried out and shown in Figure 5F,H. Obviously, E_f on the (100) and (110) surfaces is always lower than that of the corresponding interior region, or namely the bulk-like region (Figure 5F,H). These results echoed that the phase transition starts from the surface rather than the interior at a relatively low temperature. The lowest E_f on the disordered Pt_3Co (100) surface slab (−3.131 eV) is lower than that on the disordered Pt_3Co (110) surface slab (−2.861 eV) (Figure 5F,H). It is consistent with the previous analysis that the triggering of the ordering process on (110) is after that on (100).

CONCLUSIONS

In summary, our research reveals the dynamic disorder-to-order transition in the Pt_3Co NPs by observing the layer-by-layer ordering behaviors of facet alloy nanocrystals with random distribution atoms along both [100] and [110] directions at the atomic scale, involving the completion between surface diffusion and phase transition. A proper annealing process seems to be able to trigger the phase transition at the lower temperature as well as accelerate the transition *via* short-range diffusion. In addition, we discover that the ordering transition always accompanies the long-range diffusion, which seems to make the shape change inevitable. The "trade-off" between surface diffusion and reconstruction is one of the most critical steps in the preparation of the faceted preserved intermetallic-based electrocatalysts. We believe that our results provide a comprehensive atomistic-scale insight into the structural evolution during the phase transition and give ideas and suggestions on designing catalysts through the post-thermal annealing for enhanced electrocatalytic activity and durability by optimizing the surface and near-surface atomic structure. These findings would establish the foundation for surface engineering during the formation of Pt-M intermetallics and the regulation of their electrocatalytic performance. Last but not least, our work presents the *in situ* HAADF-STEM imaging technique of tracking the atomic configurations with sub-Ångström resolution.

https://dx.doi.org/10.1021/acsnano.0c10775
ACS Nano 2021, 15, 5284−5293

MATERIALS AND METHODS

Chemicals and Materials. Platinum acetylacetonate [$Pt(acac)_2$] and 2,4-pentanedione-cobalt (2:1) [$Co(acac)_2$] were purchased from Strem Chemical. Oleylamine (OAm, 80−90%) and oleic acid (OA, ≥99%) were bought from Aladdin. Chloroform and ethanol were purchased from Sinopharm Chemical Reagent Co., Ltd. All the chemicals and materials were employed as received.

Sample Preparation. Pt_3Co cube was prepared by a general gas reducing agent in liquid solution method,[35] which has been repeatedly reported. The produced NPs were washed and separated by dispersing the final reaction mixture in 2 mL of chloroform and 10 mL of ethanol, followed by centrifugation at 5000 rpm for 5 min. This procedure was repeated three times to get rid of the extra reactants and capping agents. The final products were dispersed evenly in chloroform for further *in situ* characterization.

STEM Images of *In Situ* Annealing Experiment. STEM images were performed on a JEM-ARM300F (JEOL, Tokyo, Japan) Grand ARM transmission electron microscope (TEM) equipped with two spherical aberration correctors at 300 kV. A TEM holder Fusion 200 (Protochips, North Carolina, USA) was used for controlling the *in situ* temperature during annealing. With the previous research of others, oxidizing or reducing gases will induce different types of segregation,[54] which must be eliminated in our shaped preserved phase transition. Therefore, we chose the vacuum condition to observe the *in situ* ordering behaviors at atomic resolution. The as-prepared Pt_3Co cube was dispersed in chloroform and dropped on Fusion Thermal E-chips comprised of a carbon film with 2 μm holes. The formation of intermetallic at the elevated temperature required a certain level of atom migration, which also leads to a side effect of surface geometry changes. According to the equilibrium phase diagram of bulk CoPt and nanosize effect, LTDAP and DHTAP were designed to study the formation process of intermetallic nanostructures. For LTDAP, the Pt_3Co cube was heated from RT to 300 °C using a ramping rate of 30 °C/min, and the holding time at this temperature was 60 min. With no phase transition at low temperature, the sample was heated to 600 °C using a ramping rate of 30 °C/min. The fully ordered phase was obtained after holding for 60 min at 600 °C. EDS mapping before and after annealing was acquired using JEOL's large angle silicon drift detector (SDD) EDS with a large solid angle. For DHTAP, we followed the same preparation process. The other Pt_3Co cube was heated from RT to 700 °C for 20 min using a ramping rate of 30 °C/min. All of the specimens were exposed to the electron beam only during data acquisition in order to weaken the influence of the electron beam.

S-STEM Images Simulation Method. To reveal the structure at the center of the Pt_3Co NP during LTDAP, the Pt_3Co crystal with $L1_2$ structure and six (100) surface slab models with 0, 20, 40, 60, 80, 100 atomic layers' ordering $L1_2$ structure (Figure S5) were built. Because our initial Pt_3Co NP has a cubic shape with a side length of ∼18 nm, which is ∼100 atomic layers of Pt_3Co (100), we select 100 atomic layers to simulate these dynamic growing structures, supposing the growth on six (100) surfaces is simultaneous. The ordering $L1_2$ structure is put on the surface of (100), and the Pt layers are used to represent the disordering FCC structure to fade the brightness change more violently. All of these models were fed to QSTEM, a code for simulating TEM and STEM images, to generate the representative HAADF-STEM images. A square area of the atoms in the [100] zone axis direction was scanned for each model to get the corresponding S-STEM images (Figure S5 and Figure 1). Obviously, the brightness of the Co site becomes darker and darker with the increase in thickness of the ordering $L1_2$ structure.

Calculation of the {100} Facet Preserved Ratio in View of the 2D Model. Since the initial shape of our samples is a cube enclosed by 6 {100} facets, the {100} facet remaining ratio is a good descriptor to compare these two thermal annealing methods. Therefore, we defined a parameter, {100} facet preserved ratio in view of the 2D model, to quantify the {100} facet-remaining ratio. As is shown in the following Figure S20, the 4 sides along the remaining {100} were extended and intersected into a rectangle, whose length was regarded as the denominator. Clearly, the remaining length of along {100} facet was regarded as the numerator. In this way, the shape-controlled phase transition behaviors on the {100} surface could be quantified based on the assumption that the other two sides have the same behaviors as the side we have seen. Finally, the {100} facet preserved ratio in view of the 2D model for products under LTDAP is 32.63% and that for products under DHTAP is 48.02% (Figure S20).

Calculation of the {100} Facet Preserved Ratio in View of the 3D Model. To improve the quantification accuracy toward the calculation of the {100} facet preserved ratio, we quantified it in view of the 3D model. We built a simple obtuse cube to model the products after thermal annealing (Figure S21). The initial complete area of the {100} facet can be calculated based on the parameters of a_0, b_0, and c_0, while the remaining area of the {100} facet can also be calculated based on the parameters of a_1, b_1, and c_1. Therefore, the {100} facet preserved ratio in view of the 3D model, α, can be calculated as the following:

$$\alpha = (2a_0 \times b_0 + 2a_0 \times c_0 + 2b_0 \times c_0) / (2a_1 \times b_1 + 2a_1 \times c_1 + 2b_1 \times c_1) \times 100\%$$

Since the HAADF-STEM images only exhibit the information from the 2D view (a_0, b_0, a_1, and b_1), we suppose that c_0 and c_1 are approximately equal to b_0 and b_1, separately. As a result, the {100} facet preserved ratio in view of the 3D model for products under LTDAP is 9.58% and that for products under DHTAP is 25.83% using the parameter read from Figure S20. One minor detail is that we use the average length of the two corresponding sides to represent a_1 and b_1.

DFT Simulation Method. DFT calculations using the projector augmented wave method[55] with a kinetic energy cutoff of 520 eV was performed in the Vienna *ab initio* simulation package.[56,57] The generalized gradient approximation[58] with the Perdew−Burke−Ernzerhof[59] exchange−correlation functional was applied in our calculations. A 1 × 1 × 1 conventional cell containing 4 atoms (Figure 5A) was used to model the ordered $L1_2$ Pt_3Co bulk phase. Two kinds of (100) surface slabs and two kinds of (110) surface slabs with nine atomic layers (Figure S22) were built for the ordered Pt_3Co phase. A 2 × 2 × 2 FCC supercell containing 32 atoms (Figure 5B) was adopted to model the solid solution of Pt_3Co, whose random structure was generated by following the recipes of Monte Carlo special quasi-random structure[60] within the ATAT codes.[61] We cleaved all the possible (100) and (110) surfaces (Figures S23 and S24) for the disordered Pt_3Co NP. A vacuum region of 10.0 Å thick was added between these periodic slabs. The energy convergence criterion is 0.0001 eV/atom for electronic minimization steps.

The Surface Energy. The stability of each surface energy (E) can be calculated as

$$E = [E_{slab} - (n_{Pt} - 3n_{Co})\mu_{Pt} - n_{Co}E_{Pt3Co}]/2A$$

where E_{slab} is the DFT calculated energy of the slab, n_{Pt} and n_{Co} are the numbers of the Pt and Co atoms respectively, μ_{Pt} is the chemical potential of the Pt of the surface slab and is utilized as the variable, and A is the area of the surface.[62] In our experiment, the chemical potential μ_{Pt} ranged from −5.5 eV (Pt atoms in FCC bulk) to −4.5 eV (Pt atoms on the {100} surface).[45] The DFT calculated surface energies of all possible {100} and {110} surfaces of ordered and disordered Pt_3Co are displayed in Figure S25. Obviously, Order-Pt_3Co-100-Pt, Order-Pt_3Co-110-Pt, disorder-Pt_3Co-100-4, and dis-order-Pt_3Co-110-4 display the lowest surface energy among their respective possible {100} and {110} surface configurations in the range of μ_{Pt} considered here.

The Vacancy Formation Energy. We calculated the respective vacancy formation energy because lower vacancy formation energies will promote interdiffusion of the constituent atoms *via* a vacancy diffusion mechanism.[53] We first calculated the vacancy formation energy (E_f) of Pt atom and Co atom in disordered Pt_3Co bulk phase. As far as the Co vacancy is concerned, we calculated all of the possible Co vacancy (8 in total, Figure S26A). As for the Pt vacancy, we

https://dx.doi.org/10.1021/acsnano.0c10775
ACS Nano 2021, 15, 5284−5293

calculated 8 approximately symmetrical sites (Figure S26B). The Pt vacancy formation energy was calculated as follow:

$$E_f = E_v - E_{Pt_3Co} + \mu_{Pt}$$

where E_v is the DFT calculated energy of the corresponding disordered Pt_3Co bulk with a Pt vacancy, E_{Pt_3Co} is the energy of the perfect disordered Pt_3Co bulk, and μ_{Pt} is the chemical potential energy of Pt.[63] And the Co vacancy formation energy could be defined as

$$E_f = E_v - E_{Pt_3Co} + \mu_{Co} = E_v - E_{Pt_3Co} + (E_{Pt_3Co} - 3\mu_{Pt})$$

where μ_{Co} is the chemical potential energy of Co and E_{Pt3Co} is the total energy of Pt_3Co. All possible results in Figure S27A indicate that the Co vacancy is easier to form in this disordered Pt_3Co system. Therefore, we carried out the vacancy formation energy within disordered Pt_3Co (100) and (110) surface slabs based on the Co vacancy. Their corresponding possible vacancy positions are labeled in Figure S26C,D. The dependence of the calculated E_f for Co vacancy on the μ_{Pt} is exhibited in Figure S27B,C.

ASSOCIATED CONTENT

Supporting Information

The Supporting Information is available free of charge at https://pubs.acs.org/doi/10.1021/acsnano.0c10775.

Morphology and element distribution characterization, QSTEM simulation results, alignment example, the interstitial space calculation, atomic profile analysis, facet preserved ratio, surface slab models, surface stability, the possible vacancy positions, vacancy formation energy, and the growth rate (PDF)

AUTHOR INFORMATION

Corresponding Authors

Jianbo Wu − *State Key Laboratory of Metal Matrix Composites, School of Materials Science and Engineering, Center of Hydrogen Science, and Materials Genome Initiative Center, Shanghai Jiao Tong University, Shanghai 200240, China*; orcid.org/0000-0002-3574-5585; Email: jianbowu@sjtu.edu.cn

Hong Zhu − *State Key Laboratory of Metal Matrix Composites, School of Materials Science and Engineering, University of Michigan − Shanghai Jiao Tong University Joint Institute, and Materials Genome Initiative Center, Shanghai Jiao Tong University, Shanghai 200240, China*; orcid.org/0000-0001-7919-5661; Email: hong.zhu@sjtu.edu.cn

Authors

Fan Li − *State Key Laboratory of Metal Matrix Composites, School of Materials Science and Engineering, Shanghai Jiao Tong University, Shanghai 200240, China*

Yuan Zong − *State Key Laboratory of Metal Matrix Composites, School of Materials Science and Engineering, Shanghai Jiao Tong University, Shanghai 200240, China*

Yanling Ma − *State Key Laboratory of Metal Matrix Composites, School of Materials Science and Engineering, Shanghai Jiao Tong University, Shanghai 200240, China*

Mingxu Wang − *State Key Laboratory of Metal Matrix Composites, School of Materials Science and Engineering, Shanghai Jiao Tong University, Shanghai 200240, China*

Wen Shang − *State Key Laboratory of Metal Matrix Composites, School of Materials Science and Engineering, Shanghai Jiao Tong University, Shanghai 200240, China*; orcid.org/0000-0002-6984-3060

Peng Tao − *State Key Laboratory of Metal Matrix Composites, School of Materials Science and Engineering, Shanghai Jiao Tong University, Shanghai 200240, China*; orcid.org/0000-0002-9284-7158

Chengyi Song − *State Key Laboratory of Metal Matrix Composites, School of Materials Science and Engineering, Shanghai Jiao Tong University, Shanghai 200240, China*; orcid.org/0000-0002-4757-9481

Tao Deng − *State Key Laboratory of Metal Matrix Composites, School of Materials Science and Engineering and Center of Hydrogen Science, Shanghai Jiao Tong University, Shanghai 200240, China*; orcid.org/0000-0002-1560-3838

Complete contact information is available at: https://pubs.acs.org/10.1021/acsnano.0c10775

Notes

The authors declare no competing financial interest.

ACKNOWLEDGMENTS

The work is sponsored by the thousand talents program for distinguished young scholars from the Chinese government, National Key R&D Program of China (No. 2017YFB0406000), the National Natural Science Foundation of China (21875137, 51521004, and 51420105009), start-up fund (J.W.), the Zhi-Yuan Endowed fund (T.D.), and the support from Center of Hydrogen Science and Joint Research Center for Clean Energy Materials from Shanghai Jiao Tong University. H.Z. acknowledges the financial support from Shanghai Automotive Industry Corporation (1714) and the computing resources from Shanghai Jiao Tong University Supercomputer Center. We thank Mr. Tianjiao Xin from Shanghai Institute of Microsystem and Information Technology (SIMIT) for his help on STEM images.

REFERENCES

(1) Wang, X. X.; Swihart, M. T.; Wu, G. Achievements, Challenges and Perspectives on Cathode Catalysts in Proton Exchange Membrane Fuel Cells for Transportation. *Nat. Catal.* **2019**, *2*, 578−589.

(2) Yan, Y.; Du, J. S.; Gilroy, K. D.; Yang, D.; Xia, Y.; Zhang, H. Intermetallic Nanocrystals: Syntheses and Catalytic Applications. *Adv. Mater.* **2017**, *29*, 1605997.

(3) Gamler, J. T. L.; Ashberry, H. M.; Skrabalak, S. E.; Koczkur, K. M. Random Alloyed *versus* Intermetallic Nanoparticles: A Comparison of Electrocatalytic Performance. *Adv. Mater.* **2018**, *30*, 1801563.

(4) Zhang, N.; Chen, X.; Lu, Y.; An, L.; Li, X.; Xia, D.; Zhang, Z.; Li, J. Nano-Intermetallic $AuCu_3$ Catalyst for Oxygen Reduction Reaction: Performance and Mechanism. *Small* **2014**, *10*, 2662−9.

(5) Xiao, W.; Cordeiro, M. A. L.; Gao, G.; Zheng, A.; Wang, J.; Lei, W.; Gong, M.; Lin, R.; Stavitski, E.; Xin, H. L.; Wang, D. Atomic Rearrangement from Disordered to Ordered Pd-Fe Nanocatalysts with Trace Amount of Pt Decoration for Efficient Electrocatalysis. *Nano Energy* **2018**, *50*, 70−78.

(6) Wang, Y.; Zou, L.; Huang, Q.; Zou, Z.; Yang, H. 3D Carbon Aerogel-Supported PtNi Intermetallic Nanoparticles with High Metal Loading as a Durable Oxygen Reduction Electrocatalyst. *Int. J. Hydrogen Energy* **2017**, *42*, 26695−26703.

(7) Wang, D.; Xin, H. L.; Hovden, R.; Wang, H.; Yu, Y.; Muller, D. A.; DiSalvo, F. J.; Abruna, H. D. Structurally Ordered Intermetallic Platinum-Cobalt Core-Shell Nanoparticles with Enhanced Activity and Stability as Oxygen Reduction Electrocatalysts. *Nat. Mater.* **2013**, *12*, 81−7.

(8) Leonard, B. M.; Zhou, Q.; Wu, D.; DiSalvo, F. J. Facile Synthesis of PtNi Intermetallic Nanoparticles: Influence of Reducing Agent and

Precursors on Electrocatalytic Activity. *Chem. Mater.* **2011**, *23*, 1136−1146.
(9) Kuttiyiel, K. A.; Sasaki, K.; Su, D.; Wu, L.; Zhu, Y.; Adzic, R. R. Gold-Promoted Structurally Ordered Intermetallic Palladium Cobalt Nanoparticles for the Oxygen Reduction Reaction. *Nat. Commun.* **2014**, *5*, 5185.
(10) Kim, H. Y.; Cho, S.; Sa, Y. J.; Hwang, S. M.; Park, G. G.; Shin, T. J.; Jeong, H. Y.; Yim, S. D.; Joo, S. H. Self-Supported Mesostructured Pt-Based Bimetallic Nanospheres Containing an Intermetallic Phase as Ultrastable Oxygen Reduction Electrocatalysts. *Small* **2016**, *12*, 5347−5353.
(11) Gong, M.; Deng, Z.; Xiao, D.; Han, L.; Zhao, T.; Lu, Y.; Shen, T.; Liu, X.; Lin, R.; Huang, T.; Zhou, G.; Xin, H.; Wang, D. One-Nanometer-Thick Pt_3Ni Bimetallic Alloy Nanowires Advanced Oxygen Reduction Reaction: Integrating Multiple Advantages into One Catalyst. *ACS Catal.* **2019**, *9*, 4488−4494.
(12) Cheng, N.; Zhang, L.; Mi, S.; Jiang, H.; Hu, Y.; Jiang, H.; Li, C. $L1_2$ Atomic Ordered Substrate Enhanced Pt-Skin Cu_3Pt Catalyst for Efficient Oxygen Reduction Reaction. *ACS Appl. Mater. Interfaces* **2018**, *10*, 38015−38023.
(13) Kim, J.; Lee, Y.; Sun, S. Structurally Ordered FePt Nanoparticles and Their Enhanced Catalysis for Oxygen Reduction Reaction. *J. Am. Chem. Soc.* **2010**, *132*, 4996−4997.
(14) Wang, Y.; Sun, D.; Chowdhury, T.; Wagner, J. S.; Kempa, T. J.; Hall, A. S. Rapid Room-Temperature Synthesis of a Metastable Ordered Intermetallic Electrocatalyst. *J. Am. Chem. Soc.* **2019**, *141*, 2342−2347.
(15) Li, J.; Sharma, S.; Liu, X.; Pan, Y.-T.; Spendelow, J. S.; Chi, M.; Jia, Y.; Zhang, P.; Cullen, D. A.; Xi, Z. J. J.; et al. Hard-Magnet $L1_0$-CoPt Nanoparticles Advance Fuel Cell Catalysis. *Joule* **2019**, *3*, 124−135.
(16) Li, J.; Xi, Z.; Pan, Y.-T.; Spendelow, J. S.; Duchesne, P. N.; Su, D.; Li, Q.; Yu, C.; Yin, Z.; Shen, B.; et al. Fe Stabilization by Intermetallic $L1_0$-FePt and Pt Catalysis Enhancement in $L1_0$-FePt/Pt Nanoparticles for Efficient Oxygen Reduction Reaction in Fuel Cells. *J. Am. Chem. Soc.* **2018**, *140*, 2926−2932.
(17) Bu, L.; Zhang, N.; Guo, S.; Zhang, X.; Li, J.; Yao, J.; Wu, T.; Lu, G.; Ma, J.-Y.; Su, D.; et al. Biaxially Strained PtPb/Pt Core/Shell Nanoplate Boosts Oxygen Reduction Catalysis. *Science* **2016**, *354*, 1410−1414.
(18) Menezes, P. W.; Indra, A.; Bergmann, A.; Chernev, P.; Walter, C.; Dau, H.; Strasser, P.; Driess, M. Uncovering the Prominent Role of Metal Ions in Octahedral *versus* Tetrahedral Sites of Cobalt-Zinc Oxide Catalysts for Efficient Oxidation of Water. *J. Mater. Chem. A* **2016**, *4*, 10014−10022.
(19) Xiao, W.; Lei, W.; Wang, J.; Gao, G.; Zhao, T.; Cordeiro, M. A. L.; Lin, R.; Gong, M.; Guo, X.; Stavitski, E.; Xin, H. L.; Zhu, Y.; Wang, D. Tuning the Electrocatalytic Activity of Pt by Structurally Ordered PdFe/C for the Hydrogen Oxidation Reaction in Alkaline Media. *J. Mater. Chem. A* **2018**, *6*, 11346−11352.
(20) Tran, K.; Ulissi, Z. W. Active Learning across Intermetallics to Guide Discovery of Electrocatalysts for Co_2 Reduction and H_2 Evolution. *Nat. Catal.* **2018**, *1*, 696−703.
(21) Guozhong, C. *Nanostructures and Nanomaterials: Synthesis, Properties and Applications*; World scientific: London, 2004.
(22) Avouris, P. *Atomic and Nanometer-Scale Modification of Materials: Fundamentals and Applications*; Springer Science & Business Media: New York, 2012.
(23) Kaptay, G. Nano-Calphad: Extension of the Calphad Method to Systems with Nano-Phases and Complexions. *J. Mater. Sci.* **2012**, *47*, 8320−8335.
(24) Kaatz, F. H.; Bultheel, A. Size, Shape, and Compositional Effects on the Order-Disorder Phase Transitions in Au-Cu and Pt-M (M = Fe, Co, and Ni) Nanocluster Alloys. *Nanotechnology* **2018**, *29*, 345701.
(25) Alloyeau, D.; Ricolleau, C.; Mottet, C.; Oikawa, T.; Langlois, C.; Le Bouar, Y.; Braidy, N.; Loiseau, A. Size and Shape Effects on the Order-Disorder Phase Transition in CoPt Nanoparticles. *Nat. Mater.* **2009**, *8*, 940−6.
(26) Heo, J.; Torres, D. D.; Banerjee, P.; Jain, P. K. *In-Situ* Electron Microscopy Mapping of an Order-Disorder Transition in a Superionic Conductor. *Nat. Commun.* **2019**, *10*, 1505.
(27) Rößner, L.; Armbrüster, M. Electrochemical Energy Conversion on Intermetallic Compounds: A Review. *ACS Catal.* **2019**, *9*, 2018−2062.
(28) Liang, J.; Miao, Z.; Ma, F.; Pan, R.; Chen, X.; Wang, T.; Xie, H.; Li, Q. Enhancing Oxygen Reduction Electrocatalysis through Tuning Crystal Structure: Influence of Intermetallic MPt Nanocrystals. *Chin. J. Catal.* **2018**, *39*, 583−589.
(29) Marakatti, V. S.; Peter, S. C. Synthetically Tuned Electronic and Geometrical Properties of Intermetallic Compounds as Effective Heterogeneous Catalysts. *Prog. Solid State Chem.* **2018**, *52*, 1−30.
(30) Liang, J.; Ma, F.; Hwang, S.; Wang, X.; Sokolowski, J.; Li, Q.; Wu, G.; Su, D. Atomic Arrangement Engineering of Metallic Nanocrystals for Energy-Conversion Electrocatalysis. *Joule* **2019**, *3*, 956−991.
(31) Porter, N. S.; Wu, H.; Quan, Z.; Fang, J. Shape-Control and Electrocatalytic Activity-Enhancement of Pt-Based Bimetallic Nanocrystals. *Acc. Chem. Res.* **2013**, *46*, 1867−1877.
(32) Kang, Y.; Pyo, J. B.; Ye, X.; Gordon, T. R.; Murray, C. B. Synthesis, Shape Control, and Methanol Electro-Oxidation Properties of Pt-Zn Alloy and Pt_3Zn Intermetallic Nanocrystals. *ACS Nano* **2012**, *6*, 5642−5647.
(33) An, K.; Somorjai, G. A. Size and Shape Control of Metal Nanoparticles for Reaction Selectivity in Catalysis. *ChemCatChem* **2012**, *4*, 1512−1524.
(34) Wu, J.; Zhang, J.; Peng, Z.; Yang, S.; Wagner, F. T.; Yang, H. Truncated Octahedral Pt_3Ni Oxygen Reduction Reaction Electrocatalysts. *J. Am. Chem. Soc.* **2010**, *132*, 4984−4985.
(35) Wu, J.; Gross, A.; Yang, H. Shape and Composition-Controlled Platinum Alloy Nanocrystals Using Carbon Monoxide as Reducing Agent. *Nano Lett.* **2011**, *11*, 798−802.
(36) Wu, J.; Qi, L.; You, H.; Gross, A.; Li, J.; Yang, H. Icosahedral Platinum Alloy Nanocrystals with Enhanced Electrocatalytic Activities. *J. Am. Chem. Soc.* **2012**, *134*, 11880−3.
(37) Kang, Y.; Murray, C. B. Synthesis and Electrocatalytic Properties of Cubic MnPt Nanocrystals (Nanocubes). *J. Am. Chem. Soc.* **2010**, *132*, 7568−7569.
(38) Chi, M.; Wang, C.; Lei, Y.; Wang, G.; Li, D.; More, K. L.; Lupini, A.; Allard, L. F.; Markovic, N. M.; Stamenkovic, V. R. Surface Faceting and Elemental Diffusion Behaviour at Atomic Scale for Alloy Nanoparticles During *in Situ* Annealing. *Nat. Commun.* **2015**, *6*, 8925.
(39) Le Bouar, Y.; Loiseau, A.; Finel, A. Origin of the Complex Wetting Behavior in Co-Pt Alloys. *Phys. Rev. B: Condens. Matter Mater. Phys.* **2003**, *68*, 224203.
(40) Okamoto, H. Co-Pt (Cobalt-Platinum). *J. Phase Equilib.* **2001**, *22*, 591−591.
(41) Andreazza, P.; Pierron-Bohnes, V.; Tournus, F.; Andreazza-Vignolle, C.; Dupuis, V. Structure and Order in Cobalt/Platinum-Type Nanoalloys: From Thin Films to Supported Clusters. *Surf. Sci. Rep.* **2015**, *70*, 188−258.
(42) Abild-Pedersen, F.; Greeley, J.; Studt, F.; Rossmeisl, J.; Munter, T. R.; Moses, P. G.; Skulason, E.; Bligaard, T.; Norskov, J. K. Scaling Properties of Adsorption Energies for Hydrogen-Containing Molecules on Transition-Metal Surfaces. *Phys. Rev. Lett.* **2007**, *99*, 016105.
(43) Dai, S.; You, Y.; Zhang, S.; Cai, W.; Xu, M.; Xie, L.; Wu, R.; Graham, G. W.; Pan, X. *In Situ* Atomic-Scale Observation of Oxygen-Driven Core-Shell Formation in Pt_3Co Nanoparticles. *Nat. Commun.* **2017**, *8*, 204.
(44) Wang, X. X.; Hwang, S.; Pan, Y. T.; Chen, K.; He, Y.; Karakalos, S.; Zhang, H.; Spendelow, J. S.; Su, D.; Wu, G. Ordered Pt_3Co Intermetallic Nanoparticles Derived from Metal-Organic Frameworks for Oxygen Reduction. *Nano Lett.* **2018**, *18*, 4163−4171.
(45) Dai, S.; Hou, Y.; Onoue, M.; Zhang, S.; Gao, W.; Yan, X.; Graham, G. W.; Wu, R.; Pan, X. Revealing Surface Elemental Composition and Dynamic Processes Involved in Facet-Dependent Oxidation of Pt_3Co Nanoparticles *via in Situ* Transmission Electron Microscopy. *Nano Lett.* **2017**, *17*, 4683−4688.

https://dx.doi.org/10.1021/acsnano.0c10775
ACS Nano 2021, 15, 5284−5293

(46) Jackson, K. A. *Kinetic Processes: Crystal Growth, Diffusion, and Phase Transformations in Materials*; John Wiley & Sons: Prescott Arizona, 2006.
(47) Blatov, V. A.; Golov, A. A.; Yang, C.; Zeng, Q.; Kabanov, A. A. Network Topological Model of Reconstructive Solid-State Transformations. *Sci. Rep.* **2019**, *9*, 6007.
(48) Holovatch, Y. *Order, Disorder and Criticality: Advanced Problems of Phase Transition Theory*; World Scientific: Ukraine, 2004.
(49) Li, Q.; Wu, L.; Wu, G.; Su, D.; Lv, H.; Zhang, S.; Zhu, W.; Casimir, A.; Zhu, H.; Mendoza-Garcia, A.; Sun, S. New Approach to Fully Ordered Fct-FePt Nanoparticles for Much Enhanced Electrocatalysis in Acid. *Nano Lett.* **2015**, *15*, 2468−73.
(50) Rong, H.; Mao, J.; Xin, P.; He, D.; Chen, Y.; Wang, D.; Niu, Z.; Wu, Y.; Li, Y. Kinetically Controlling Surface Structure to Construct Defect-Rich Intermetallic Nanocrystals: Effective and Stable Catalysts. *Adv. Mater.* **2016**, *28*, 2540−6.
(51) Askeland, D. R.; Phule, P. P. *The Science and Engineering of Materials*; Springer: New York, 2003.
(52) Callister, W. D. *Fundamentals of Materials Science and Engineering*. Wiley: London, 2000.
(53) Sun, D.; Wang, Y.; Livi, K. J.; Wang, C.; Luo, R.; Zhang, Z.; Alghamdi, H.; Li, C.; An, F.; Gaskey, B.; et al. Ordered Intermetallic Pd_3Bi Ordered Intermetallic Pd $_3$ Bi Prepared by an Electrochemically Induced Phase Transformation for Oxygen Reduction Electrocatalysis. *ACS Nano* **2019**, *13*, 10818−10825.
(54) Tao, F.; Grass, M. E.; Zhang, Y.; Butcher, D. R.; Renzas, J. R.; Liu, Z.; Chung, J. Y.; Mun, B. S.; Salmeron, M.; Somorjai, G. A. Reaction-Driven Restructuring of Rh-Pd and Pt-Pd Core-Shell Nanoparticles. *Science* **2008**, *322*, 932−934.
(55) Blöchl, P. E. Projector Augmented-Wave Method. *Phys. Rev. B: Condens. Matter Mater. Phys.* **1994**, *50*, 17953−17979.
(56) Kresse, G.; Furthmüller, J. Efficient Iterative Schemes for *ab Initio* Total-Energy Calculations Using a Plane-Wave Basis Set. *Phys. Rev. B: Condens. Matter Mater. Phys.* **1996**, *54*, 11169−11186.
(57) Kresse, G.; Hafner, J. *Ab Initio* Molecular Dynamics for Liquid Metals. *Phys. Rev. B: Condens. Matter Mater. Phys.* **1993**, *47*, 558−561.
(58) Perdew, J. P.; Chevary, J. A.; Vosko, S. H.; Jackson, K. A.; Pederson, M. R.; Singh, D. J.; Fiolhais, C. Atoms, Molecules, Solids, and Surfaces: Applications of the Generalized Gradient Approximation for Exchange and Correlation. *Phys. Rev. B: Condens. Matter Mater. Phys.* **1992**, *46*, 6671−6687.
(59) Perdew, J. P.; Burke, K.; Ernzerhof, M. Generalized Gradient Approximation Mode Simple. *Phys. Rev. Lett.* **1996**, *77*, 3865−3868.
(60) Van de Walle, A.; Tiwary, P.; De Jong, M.; Olmsted, D.; Asta, M.; Dick, A.; Shin, D.; Wang, Y.; Chen, L.-Q.; Liu, Z.-K. Efficient Stochastic Generation of Special Quasirandom Structures. *CALPHAD: Comput. Coupling Phase Diagrams Thermochem.* **2013**, *42*, 13−18.
(61) Van de Walle, A.; Asta, M.; Ceder, G. The Alloy Theoretic Automated Toolkit: A User Guide. *CALPHAD: Comput. Coupling Phase Diagrams Thermochem.* **2002**, *26*, 539−553.
(62) Wang, X. G.; Weiss, W.; Shaikhutdinov, S. K.; Ritter, M.; Petersen, M.; Wagner, F.; Schlögl, R.; Scheffler, M. The Hematite (α-Fe_2O_3) (0001) Surface: Evidence for Domains of Distinct Chemistry. *Phys. Rev. Lett.* **1998**, *81*, 1038−1041.
(63) Esfandiarpour, A.; Nasrabadi, M. N. Vacancy Formation Energy in CuNiCo Equimolar Alloy and CuNiCoFe High Entropy Alloy: *Ab Initio* Based Study. *CALPHAD: Comput. Coupling Phase Diagrams Thermochem.* **2019**, *66*, 101634.

https://dx.doi.org/10.1021/acsnano.0c10775
ACS Nano 2021, 15, 5284−5293